Chemical Science

ROYAL SOCIETY OF CHEMISTRY

EDGE ARTICLE

Diachronic evolvement from tetra-icosahedral to quasi-hexagonal close-packed bimetal clusters†

Shisi Tang,‡[a] Endong Wang,‡[b] Yanzhen Wu,‡[c] Tongxin Song,[a] Meng Zhou, [ID] *[c] Xiao Cai,[a] Yi Gao,*[b] Weiping Ding [ID] [a] and Yan Zhu [ID] *[a]

Here we report a diachronic evolvement from tetra-icosahedral $Au_{30}Ag_{12}(C\equiv CR)_{24}$ to quasi-hcp (hexagonal close-packed) $Au_{47}Ag_{19}(C\equiv CR)_{32}$ via a one-step reduction, in which the size/structure conversion of the two clusters is not a typical Oswald growth process, but involves interface shrinking followed by core rearrangement and surface polymerization. $Au_{30}Ag_{12}(C\equiv CR)_{24}$ has an aesthetic $Au_{18}Ag_8$ kernel that is composed of four interpenetrating $Au_{10}Ag_3$ icosahedra, while $Au_{47}Ag_{19}(C\equiv CR)_{32}$ has a twisted Au_{19} core capped by a $Au_{12}Ag_{19}$ shell that are stacked in a layer-by-layer manner with a quasi-hcp pattern. The discovery of the two clusters not only provides further evidence for icosahedral clusters with longer excited-state lifetime compared to hcp-like clusters, but also discloses a double increase in catalytic reactivity for electrocatalytic oxidation of ethanol over quasi-hcp clusters in comparison with icosahedral clusters. This work provides the rationale for reversing the bottom-up growth process to remake bimetal clusters.

Introduction

Atomically precise metal clusters with crystallographically solved structures are ideally composed of an exact number of metal atoms.[1-4] The knowledge gained from the study of these clusters has provided valuable information about the evolution from the metallic state to the molecular exciton state,[5,6] the origin of the chiral structure,[7] the fundamental understanding of heterogeneous catalysis[8] and so on, which are currently not available from typical nanoparticles. Recently, significant advances have been made in the precise synthesis of metal clusters, thereby building the library of metal clusters with rich size and structure diversity. The icosahedron is perhaps the most popular structure in nanoclusters. Among reported clusters, many clusters are formed from single or multiple-twinned icosahedra, such as $Au_{25}(SR)_{18}$, $Au_{38}(SR)_{24}$, $Au_{133}(SR)_{52}$, $Au_{144}(SR)_{60}$, $Au_{25}(PPh_3)_{10}(SR)_5Cl_2$, $Au_{37}(PPh_3)_{10}(SR)_{10}Cl_2$, $Au_{55}(PPh_3)_{12}Cl_6$, $Au_{60}Se_2(PPh_3)_{10}(SeR)_{15}$, $Au_{12}Ag_{60}(SR)_{31}Br_9(Dppp)_6$,

etc.[9-22] Interestingly, hcp or hcp-like structures are rarely observed in the library of clusters.[23-26] Currently, the understanding of the formation mechanism of clusters is still lacking, as it is difficult to directly observe dynamic processes of such small metal ions and ligands in the solution phase. As a result, manipulating the assembly of atoms into the target structure via the bottom-up process remains a challenge.

One alternative way to solve the issue is the interconversion strategy from the parent clusters to target structures such as hcp-like clusters, in which the atomically precise starting point with clusters can permit tracing the growth process via experiments coupled with theory. In fact, the size/structure transformation of metal clusters into another new ones is well precedented.[27-34] For example, Xie and colleagues reported a three-stage size growth mechanism from $[Au_{25}(SR)_{18}]^-$ to $[Au_{44}(SR)_{26}]^{2-}$ monitored by time-course electrospray ionization mass spectrometry (ESI-MS): kinetically controlled accumulation of Au_{25} reaction with AuSR; Au_{25}-mediated size growth with bottom-up Lamer and volcano-shaped growth patterns; thermodynamically driven size-focusing into Au_{44}.[35] Jin and colleagues proposed a shuttling-out mechanism for the formation of $[Au_{24}(PPh_3)_{10}(SR)_5Cl_2]^+$ from its parent $[Au_{25}(PPh_3)_{10}(SR)_5Cl_2]^{2+}$ based on density functional theory (DFT) simulations and ESI-MS: adsorption of a PPh_3 onto a gold atom located at the waist position to initiate the reaction; Au–S bond breaking and the gold atom at the center dislocating toward the surface; the $Au(PPh_3)_2$ moiety formed on the surface eventually detaching from the Au_{25} to result in hollow Au_{24}.[36] To enrich the metal clusters with tailored structure and functionality,

[a]*School of Chemistry and Chemical Engineering, Nanjing University, Nanjing 210093, China. E-mail: zhuyan@nju.edu.cn*

[b]*Phonon Science Research Center for Carbon Dioxide, Shanghai Advanced Research Institute, Chinese Academy of Sciences, Shanghai 201210, China. E-mail: gaoyi@sari.ac.cn*

[c]*Hefei National Research Center for Physical Sciences at the Microscale, Department of Chemical Physics, University of Science and Technology of China, Hefei 230026, China. E-mail: mzhou88@ustc.edu.cn*

‡ These authors contributed equally to this work.

a fundamental understanding of the critical growth event from non-hcp to hcp-like clusters is thus most needed.

In this study, we initially present the synthesis of an icosahedron-based $Au_{30}Ag_{12}(C{\equiv}CR)_{24}$ cluster (where $HC{\equiv}CR$ is 1-ethynyl-2,4-dimethylbenzene) through the co-reduction of the $AuC{\equiv}CR$ and $AgC{\equiv}CR$ by tert-butylamine borane ($C_4H_{11}NBH_3$). $Au_{30}Ag_{12}(C{\equiv}CR)_{24}$ contains a $Au_{18}Ag_8$ core that is fused from four $Au_{10}Ag_3$ icosahedral units. Notably, the $Au_{30}Ag_{12}(C{\equiv}CR)_{24}$ cluster is then reduced by $C_4H_{11}NBH_3$ and further transformed into a new $Au_{47}Ag_{19}(C{\equiv}CR)_{32}$ cluster with quasi-hcp structure, which is composed of a layered-like Au_{19} core encapsulated by a $Au_{12}Ag_{19}$ shell. The transformation from tetra-icosahedral $Au_{30}Ag_{12}(C{\equiv}CR)_{24}$ to quasi-hcp $Au_{47}Ag_{19}(C{\equiv}CR)_{32}$ proceeds via a stepwise mechanism, with the surface staples shrinking sequentially with the core growing. More notably, tetra-icosahedral $Au_{30}Ag_{12}(C{\equiv}CR)_{24}$ and quasi-hcp $Au_{47}Ag_{19}(C{\equiv}CR)_{32}$ show diversity in physicochemical properties pursued by our studies.

Results and discussion

The total structure of the $Au_{30}Ag_{12}(C{\equiv}CR)_{24}$ (hereafter $Au_{30}Ag_{12}$) cluster was solved by single-crystal X-ray diffraction (Table S1†). As shown in Fig. 1, $Au_{30}Ag_{12}$ has a S_4 symmetry and can be viewed as a tetra-icosahedral structure. The $Au_{18}Ag_8$ kernel in $Au_{30}Ag_{12}$ can be seen as an assembly of four icosahedral $Au_{10}Ag_3$ building blocks (Fig. 1a and S1†). Interestingly, the central atoms of the four icosahedra that are respectively marked with 1, 2, 3, 4 compose a Au_4 tetrahedron. The four icosahedra are assembled through interpenetration sharing a M_7 pentagonal bipyramid (Fig. S1†), and they are slightly distorted, which may be ascribed to the asymmetric introduction of Ag atoms into the icosahedra. The $Au_{18}Ag_8$ kernel is further stabilized by four trimeric $RC{\equiv}C$–Au–$C_2(R)$–Ag–$C_2(R)$–Au–$RC{\equiv}C$ (motifs A and B in Fig. 1b) and four monomeric $RC{\equiv}C$–Au–$C{\equiv}CR$ (motif C in Fig. 1b). In motif A, all four alkyne ligands interact with metal atoms via σ–π bonds

and the Ag atom in the middle interacts with two alkyne ligands via π bonds, while in motif B, one alkyne ligand adopts a bridge mode with only a σ interaction μ_2-η^1(Au), η^2(Ag). The chemical formula of $Au_{30}Ag_{12}(C{\equiv}CR)_{24}$ is further confirmed by ESI-MS (Fig. S2†).

Next, the $Au_{30}Ag_{12}(C{\equiv}CR)_{24}$ cluster can be further converted to another new cluster using $C_4H_{11}NBH_3$. Adding thimbleful reductant into the dichloromethane solution of $Au_{30}Ag_{12}$ clusters, the green solution turned purple tardily. We monitored the transformation process using time-resolved UV-vis adsorption spectroscopy. From Fig. 2a and S3,† after the addition of the reducing agent, the three characteristic peaks at 444, 594 and 687 nm of $Au_{30}Ag_{12}$ became weak, accompanied by the redshift of the peak at 444 nm, indicating that the cluster structure gradually dissociated. After 6 h, a peak appeared around 550 nm, gradually intensified and redshifted. At 20 h, the peak offset to around 450 nm began to intensify and continued to redshift. After 28 h, deduced from the optical absorption from the reaction solution, no significant change was observed in the range of 300–900 nm, which suggested that a new cluster was formed in the solution and finally exhibited two distinct peaks at 460 and 554 nm (Fig. 2a and S4†).

We separated and purified the transformation product to obtain the novel cluster, whose chemical formula was analyzed by matrix-assisted laser desorption ionization time of flight mass spectrometry (MALDI-TOF-MS). The two dominant broad peaks at 15.184 and 10.377 kDa were assigned to $Au_{47}Ag_{19}(C{\equiv}CR)_{30}$ (expected $m/z = 15\,184$) and $Au_{39}Ag_{19}(C{\equiv}CR)_5$ (expected $m/z = 10\,378$), respectively (Fig. S5†). Therefore, we speculated that the new cluster might contain 47 Au atoms and 19 Ag atoms (short for $Au_{47}Ag_{19}$). Moreover, MALDI-TOF-MS was performed to identify stable intermediate species during the cluster transformation. For pure $Au_{30}Ag_{12}$, MALDI-TOF-MS gave a main peak at 10.302 kDa, which matched the formula weight of $Au_{30}Ag_{12}(C{\equiv}CR)_{24}$. And two slight peaks at 9.177 and 6.230 kDa were assigned to $Au_{28}Ag_{10}(C{\equiv}CR)_{20}$ and $Au_{22}Ag_8(C{\equiv}CR)_8$, respectively (Fig. 2b and S6†). At 6 h after the addition of the reducing agent, the main peaks still existed, but a series of new peaks appeared around 9.3 kDa, corresponding to $Au_{28}Ag_{10}(C{\equiv}CR)_{20}$, $Au_{29}Ag_{11}(C{\equiv}CR)_{20}$, $Au_{28}Ag_{12}(C{\equiv}CR)_{21}$ and so on, indicating that the surface structural units of $Au_{30}Ag_{12}$ began to dissociate (Fig. 2b and S7†). At 20 h, the characteristic peak of $Au_{30}Ag_{12}$ disappeared, and peaks with smaller molecular weight appeared around 9.0 kDa and larger substances were generated: the peak at 11.059 kDa is assigned to $Au_{32}Ag_{13}(C{\equiv}CR)_{26}$, and the peak around 15.2 kDa is assigned to $Au_{47}Ag_{19}(C{\equiv}CR)_{30}$ (Fig. 2b and S8†). At 28 h, peaks around 9.0 kDa decreased and were replaced by a series of peaks around 5.5 kDa (Fig. 2b, S9–S12†). At 34 h, the characteristic peaks of the cluster and a bunch of peaks below 2.5 kDa were left, indicating that the cluster and Au-alkyne complexes were finally present in the solution.

Furthermore, the total structure of $Au_{47}Ag_{19}(C{\equiv}CR)_{32}$ was determined by single-crystal X-ray diffraction (Table S2†). As shown in Fig. 2c, the cluster is protected by 32 alkyne ligands and hence its chemical formula can be unambiguously identified as $Au_{47}Ag_{19}(C{\equiv}CR)_{32}$. Different from the parent $Au_{30}Ag_{12}$ cluster, $Au_{47}Ag_{19}$ can be viewed as a core–shell structure arranged along
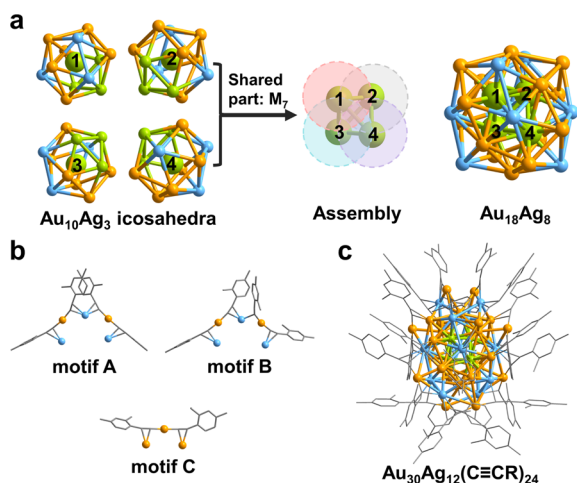

Fig. 1 (a) $Au_{18}Ag_8$ kernel formed by four interpenetrating $Au_{10}Ag_3$ icosahedra. (b) Three different motifs. (c) Total structure of $Au_{30}Ag_{12}(C{\equiv}CR)_{24}$. Color codes: orange/green, Au; blue, Ag; gray, C. The H atoms are omitted for clarity.
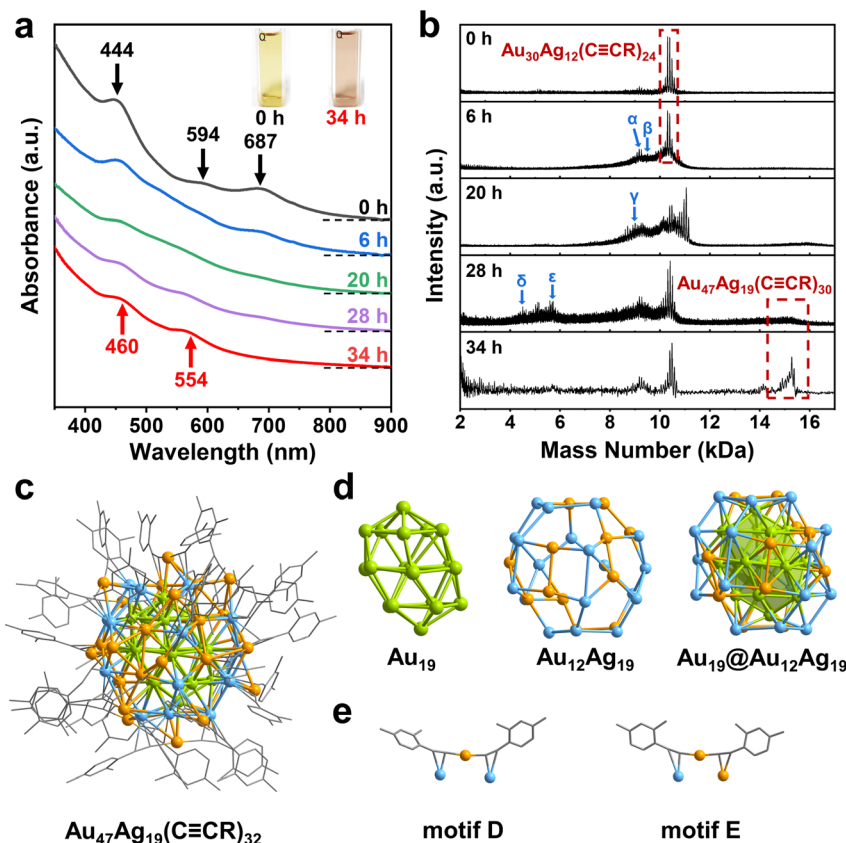
Fig. 2 (a) Time-resolved UV-vis spectra and (b) MALDI-TOF-MS spectra obtained from the transformation from $Au_{30}Ag_{12}(C\equiv CR)_{24}$ to $Au_{47}Ag_{19}(C\equiv CR)_{32}$. Formulae of intermediates captured in MALDI-TOF-MS: α, $Au_{28}Ag_{10}(C\equiv CR)_{20}$; β, $Au_{29}Ag_{11}(C\equiv CR)_{20}$; γ, $Au_{26}Ag_{12}(C\equiv CR)_{20}$; δ, $Au_{18}Ag_8$; ε, $Au_{22}Ag_8(C\equiv CR)_4$. (c) Total structure of $Au_{47}Ag_{19}(C\equiv CR)_{32}$. (d) Au_{19} core, $Au_{12}Ag_{19}$ shell and $Au_{19}@Au_{12}Ag_{19}$. (e) Two different motifs. Color codes: orange/green, Au; blue, Ag; gray, C. The H atoms are omitted for clarity.

a C_2 axis. The kernel of $Au_{47}Ag_{19}$ is a twisted Au_{19} that is dissected in a layer-by-layer manner (Fig. 2d), in which the middle layer is a regular hexagon Au_7, the two layers adjacent to the Au_7 hexagon are pentagons, and two vertex atoms at both ends. The Au_{19} kernel is surrounded by the $Au_{12}Ag_{19}$ shell. $Au_{47}Ag_{19}$ includes only monomeric $RC\equiv C-Au-C\equiv C(R)$ staples that adopt two coordination modes: μ_2-η^1(Au), η^2(Au) and μ_2-η^1(Au), η^2(Ag) (Fig. 2e). Generally, nanoclusters as large as $Au_{47}Ag_{19}$ contain basic polyhedral structural units which can be tetrahedron, icosahedron or based on fcc, hcp or bcc (body-centered cubic) arrangements. And the basic units grow into larger structures through fusion, interpenetration, shell-by-shell and layer-by-layer modes. Strictly speaking, the basic units mentioned above are not found in $Au_{47}Ag_{19}$. The Au_{19} nucleus is somewhat similar to the hcp structure, even though there is a torsion Angle between the two Au_5 layers. Therefore, the Au_{19} core can be viewed as a quasi-hcp structure whose layers are stacking in the ABABA pattern with distortion (Fig. S13†). This indicates that the tetra-icosahedral $Au_{30}Ag_{12}$ grows towards hcp during the transformation process. The two clusters are quite robust (Fig. S14†) and the in-lattice connection modes of the two clusters are shown in Fig. S15 and S16† in detail.

To elucidate the growth from $Au_{30}Ag_{12}$ to $Au_{47}Ag_{19}$, we conducted density functional theory (DFT) calculations to model the structural transformation based on the MALDI-TOF-MS experiment results. Fig. 2b illustrates that, except for the bunch of signals relating to the $Au_{30}Ag_{12}(C\equiv CR)_{24}$ cluster persisting throughout the entire transformation process, the intermediate size decreased gradually from 0–28 h, evident in the shift of the peaks. The transition from 0–28 h might signal the size decreasing period. During this period, several intermediates, including the $Au_{28}Ag_{10}(C\equiv CR)_{20}$ and $Au_{29}Ag_{11}(C\equiv CR)_{20}$ formed at 6 h, $Au_{26}Ag_{12}(C\equiv CR)_{20}$ formed at 20 h, and $Au_{22}Ag_8(C\equiv CR)_4$ and $Au_{18}Ag_8$ formed at 28 h, were notably observed with apparent intensity signals, indicating their key role in the size-decreasing process. As shown in Fig. 3a, starting from the full $Au_{30}Ag_{12}(C\equiv CR)_{24}$ cluster (isomer 1), four $HC\equiv CAuC\equiv C(H)Ag$ fragments were removed one by one with the energy preference sequence, producing the isomers from 2–5, as depicted in Fig. 3a. Among them, isomer 2 ($Au_{29}Ag_{11}(C\equiv CR)_{22}$) can transform into $Au_{29}Ag_{11}(C\equiv CR)_{20}$ via abscission of two $C\equiv CR$ fragments and isomer 3 was consistent with the intermediate $Au_{28}Ag_{10}(C\equiv CR)_{20}$ characterized at 6 h. After that, the $HC\equiv CAuC\equiv CH$ motifs were further removed stepwise, finally leaving the metal $Au_{18}Ag_8$ kernel. Among the isomers of 6–13, $Au_{24}Ag_8(C\equiv CR)_{12}$ (isomer 7), $Au_{22}Ag_8(C\equiv CR)_8$ (isomer 9), and $Au_{20}Ag_8(C\equiv CR)_4$ (isomer 11) can transform into $Au_{24}Ag_8(C\equiv CR)_0$, $Au_{22}Ag_8(C\equiv CR)_4$, and $Au_{20}Ag_8(C\equiv CR)_1$ by $C\equiv CR$
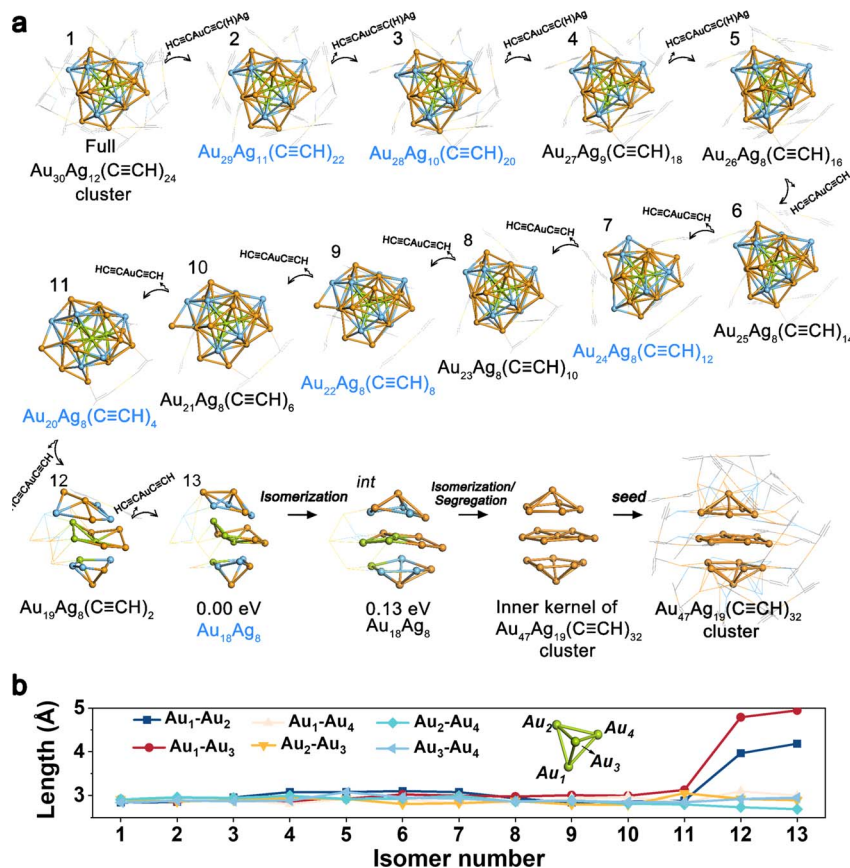
Fig. 3 (a) The proposed transformation pathway from $Au_{30}Ag_{12}(C\equiv CR)_{24}$ to the seed of the $Au_{47}Ag_{19}(C\equiv CR)_{32}$ cluster. (b) Au–Au length of the Au_4 fragment of the $Au_{30}Ag_{12}(C\equiv CR)_{24}$ cluster. Color codes: orange/green, Au; blue, Ag; gray, C. The H atoms are omitted for clarity.

abscission. These isomers confirmed the rationality of the proposed pathway.

From 28 h to 34 h, the peaks relating to the intermediates of $Au_{18}Ag_8$, $Au_{22}Ag_8(C\equiv CR)_4$ disappeared, and the peak signaling the production of the $Au_{47}Ag_{19}$ cluster emerged, implying that the generation of the $Au_{47}Ag_{19}$ cluster at 34 h originated from the intermediates of $Au_{18}Ag_8$ and $Au_{22}Ag_8(C\equiv CR)_4$ at 28 h. As mentioned above, the kernel of $Au_{30}Ag_{12}$ can be regarded as the fusion of four M_{13} fragments. The four Au atoms from each of the four M_{13} fragments constituted a central Au_4 pyramid core. Fig. 3b shows the distances of the six Au–Au bonds of the Au_4 core. For isomers 1–11, the Au–Au length did not change significantly upon the removal of the outer motifs. However, the transformation from isomer 11 to isomer 12 showed significant structural distortions. The Au_1–Au_2 and Au_1–Au_3 lengths of isomer 12 in Fig. 3b increased to 3.96 and 4.79 Å, indicating the dissociation of the central Au_4 core of the cluster and the consequent destruction of the tetra-icosahedral pattern. The transformation from isomer 12 to isomer 13, i.e., naked $Au_{18}Ag_8$ isomer, involved the continued lengthening of the Au_1–Au_2 (4.18 Å) and Au_1–Au_3 lengths (4.95 Å). The naked $Au_{18}Ag_8$ intermediate (isomer 13) can easily isomerize to an isomer intermediate with similar stability, which possessed the same packing mode as the inner kernel of the $Au_{47}Ag_{19}$ cluster. Next, the $Au_{13}Ag_6$ part of the isomer intermediate can undergo

segregation[37,38] or Au–Ag exchange with the species in the solvation environment, generating the Au_{19} species or bigger intermediates containing the Au_{19} species. This can be seen as a seed for the birth of the $Au_{47}Ag_{19}$ cluster.

The Kohn–Sham (KS) orbital energy levels and atomic orbital components in each orbital of the two clusters are shown in Fig. S17.† The main absorption peak of $Au_{30}Ag_{12}$ lies at 1.70 eV (Fig. S18†), which corresponds to the orbital transitions including HOMO−3 → LUMO+2, HOMO−1 → LUMO+3, HOMO−2 → LUMO+4 (HOMO: highest occupied molecular orbital; LUMO: lowest unoccupied molecular orbital). For $Au_{47}Ag_{19}$, the main absorption peaks are located at 1.41 and 2.31 eV, which include the orbital transitions of HOMO−6 → LUMO+2, HOMO−2 → LUMO+5 for 1.41 eV, and HOMO−48 → HOMO, HOMO−35 → LUMO+3 for 2.31 eV (Fig. S17a†), respectively. It can also be seen that the metal atoms contribute considerably to the population of the frontier orbital. Furthermore, for the $Au_{30}Ag_{12}$ cluster, the energies of the HOMO and LUMO orbitals are −5.38 and −4.41 eV, which lead to the HOMO–LUMO gap of 0.97 eV; for the $Au_{47}Ag_{19}$ cluster, the energy of the LUMO orbital slightly increases by 0.09 eV and the energy of the HOMO orbital elevates a little bit more by 0.20 eV, which eventually lowers the gap to 0.86 eV (Fig. S17b†). The transitions of molecular orbital topologies from the HOMO to the LUMO of the two clusters show different trends for their populations. For the $Au_{30}Ag_{12}$

cluster, the population of the orbital seems to narrow on the metal core from the HOMO orbital to the LUMO orbital. However, for the $Au_{47}Ag_{19}$ cluster, the LUMO orbital slightly extends to the outer ligands. From the UV-vis-NIR absorption spectra in the photon energy scale, the optical energy gaps of the $Au_{30}Ag_{12}$ and $Au_{47}Ag_{19}$ are determined as 0.89 and 0.82 eV, respectively (Fig. S19†). For the Square wave voltammetry (SWV) curves, there is an oxidation peak at 0.70 V (O1) and two reduction peaks at -0.05 V (R1) and -0.75 V (R2) for $Au_{30}Ag_{12}$, and there is an oxidation peak at 0.77 V (O1) and two reduction peaks at 0.07 V (R1) and -0.79 V (R2) for $Au_{47}Ag_{19}$. Therefore, the electrochemical energy gaps are calculated to be 0.75 eV for $Au_{30}Ag_{12}$ and 0.70 eV for $Au_{47}Ag_{19}$ (Fig. S19†).

The $Au_{30}(SR)_{18}$ with a hcp pattern was previously reported to give rise to a very short excited-state lifetime due to the close packing structure.[39] With the two clusters in hand, a question was whether quasi-hcp $Au_{47}Ag_{19}$ was used to further justify the shorter TA lifetime of hcp-like clusters than non-hcp clusters. We investigated the excited-state dynamics of the two clusters by performing time-resolved transient absorption spectroscopy (TAS). Fig. 4a and b show the femtosecond (fs) TA data map of $Au_{30}Ag_{12}$ and $Au_{47}Ag_{19}$ with excitation at 380 nm (3.26 eV). Between 0.1 and 1 ps, one can observe ultrafast relaxation of excited state absorption (ESA) in both the NCs, which was rapid relaxation from higher to lower excited states. Between 1 ps and 2 ns, the TA signals (both ESA and GSB) of $Au_{30}Ag_{12}$ decayed to

half of its maximum while the TA signals of $Au_{47}Ag_{19}$ decayed to zero. Fig. 4c shows the fs-TA kinetic traces and fittings of the two clusters probed at 630 nm, and the fitting parameters are shown in Table S3.† Since the TA signal of $Au_{30}Ag_{12}$ did not decay to zero at 2 ns, we performed nanosecond TA under the same experimental conditions (Fig. S20†). In contrast to $Au_{30}Ag_{12}$ that showed single exponential decay after 5 ps, $Au_{47}Ag_{19}$ exhibited two-exponential nanosecond decay in both GSB and ESA kinetics. The average excited state lifetime was fitted to be 2.5 ns for $Au_{30}Ag_{12}$ and 0.86 ns for $Au_{47}Ag_{19}$ (Fig. 4c and d), which was in full agreement with reported results. The shorter exciton lifetime in $Au_{47}Ag_{19}$ should also be ascribed to the stronger overlap of the HOMO and LUMO because of the close packed mode of the metal core.[40,41]

We next sought to explore the catalytic properties of $Au_{30}Ag_{12}$ and $Au_{47}Ag_{19}$. As presented in Fig. 5a, using electrocatalytic oxidation of ethanol (EOR) toward CH_3COOH as a probe reaction (Fig. S21†), the $Au_{47}Ag_{19}$ catalyst exhibited over 2-fold increase in the EOR current in 1 M KOH + 1 M CH_3CH_2OH solution, compared to the $Au_{30}Ag_{12}$ catalyst. The mass activities of $Au_{30}Ag_{12}$ and $Au_{47}Ag_{19}$ were 111.2 and 242.5 mA/mg$_{AuAg}$ at a cell voltage of 0.08 V vs. Ag/AgCl, respectively. As for the onset potential, $Au_{47}Ag_{19}$ also showed a significant negative shift (Fig. 5a). The electrochemically active surface areas (ECSAs) of $Au_{30}Ag_{12}$ and $Au_{47}Ag_{19}$ were measured to be 8.57 and 17.39 cm^2/mg$_{AuAg}$, respectively, based on the cyclic voltammogram curves

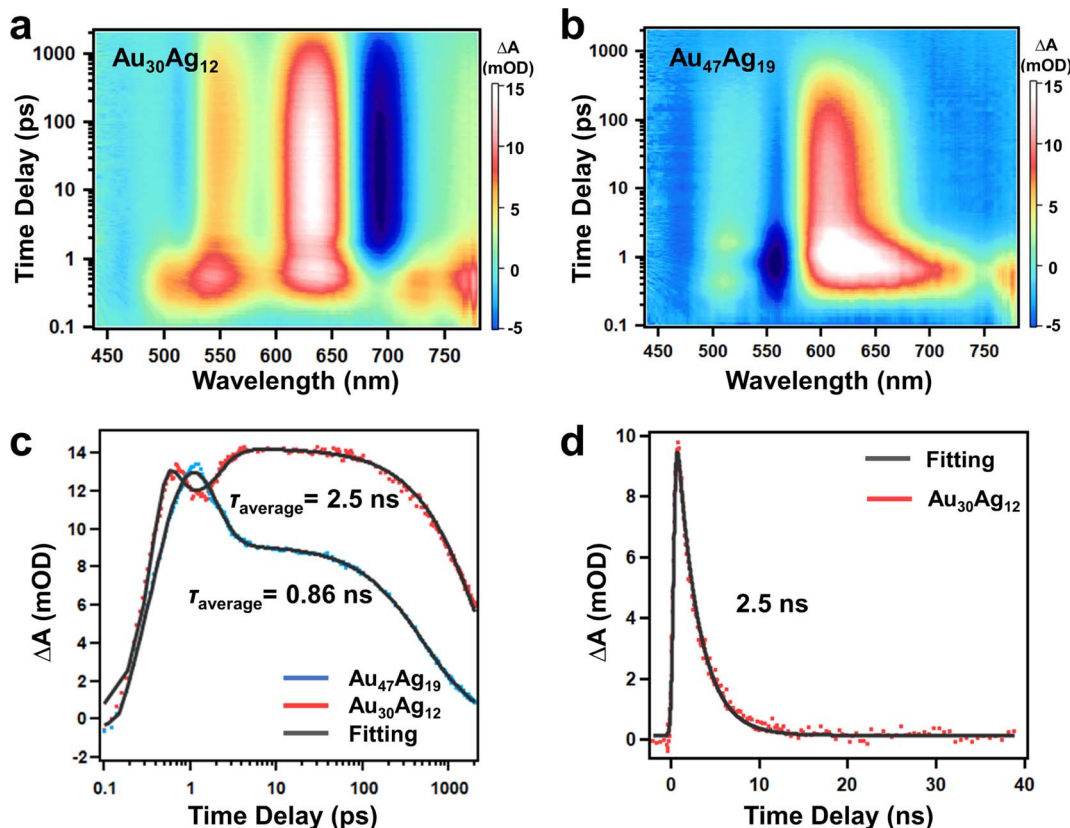**Fig. 4** Fs-TA data map of (a) $Au_{30}Ag_{12}$ and (b) $Au_{47}Ag_{19}$ with excitation at 380 nm. (c) Comparison of TA kinetic traces and fittings probed at 630 nm of two NCs. (d) Ns-TA kinetics traces of $Au_{30}Ag_{12}$ probed at 630 nm and corresponding fit.
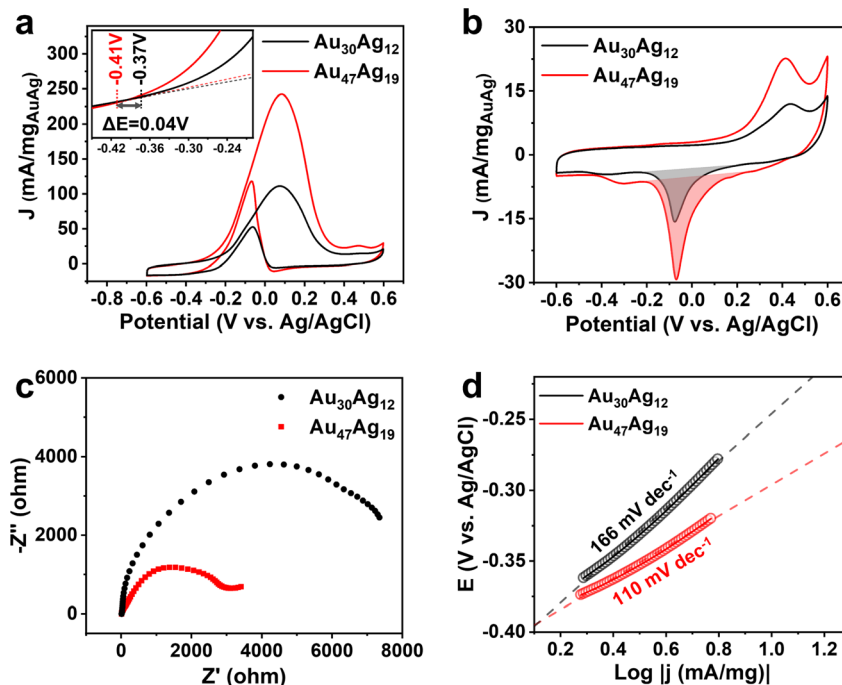
Fig. 5 (a) CVs of the $Au_{30}Ag_{12}$ and $Au_{47}Ag_{19}$ catalysts in 1 M KOH and 1 M CH_3CH_2OH solution. (b) CVs of the two catalysts in 1 M KOH solution and the shaded areas are used to calculate the ECSAs. (c) Electrochemical impedance spectra and (d) Tafel plots for EOR obtained on the two catalysts.

(CVs) in Fig. 5b. Thus, the specific activities of EOR at 0.08 V *vs.* Ag/AgCl by normalizing ECSAs were 13.94 mA cm^{-2} for $Au_{47}Ag_{19}$ and 12.97 mA cm^{-2} for $Au_{30}Ag_{12}$ (Fig. S22†). Electrochemical impedance spectroscopy (EIS) was carried out at 0.08 V *vs.* Ag/AgCl. In Fig. 5c, $Au_{47}Ag_{19}$ possessed a much smaller semi-circle diameter than $Au_{30}Ag_{12}$, suggesting that the former had better conductivity and smaller electron transfer resistance, which was consistent with better EOR performance of the $Au_{47}Ag_{19}$ catalyst. Fig. 5d shows that the Tafel slope of $Au_{47}Ag_{19}$ was obviously lower than that of $Au_{30}Ag_{12}$, indicating that the current density of $Au_{47}Ag_{19}$ increased faster, thereby showing better efficiency in EOR.

DFT calculations were performed to further shed light on the mechanism of the electrocatalytic oxidation of ethanol on the two catalysts. Previous studies have suggested that the oxidation reaction from CH_3CH_2OH to CH_3COOH can proceed *via* the adsorption of the α-C atom or O atom of CH_3CH_2OH.[42,43] The adsorption of the O atom was adopted in this work because the adsorption of the α-C atom, which was similar to quasi-horizontal placement of the CH_3CH_2OH, needs to overcome a larger steric effect with respect to the adsorption of the O atom, *i.e.*, vertical placement of CH_3CH_2OH, due to the presence of the surface ligands. Due to the symmetry of $Au_{30}Ag_{12}$, five possible reactive sites can be found as in Fig. S23a.† The O–H scission was considered, which had the largest Gibbs free energy change (ΔG; Fig. S24†). Considering the computational cost, the electronic energy change of this step was used for screening the reactive sites (Fig. S23a†). Upon the adsorption of the CH_3CH_2OH on the surface of the $Au_{30}Ag_{12}$ cluster, the reaction initiated *via* the removal of the H atom from the –OH

group of the adsorbed CH_3CH_2OH molecule, which had 0.79 eV increment of ΔG (Fig. S24†). Then, the H atom from the α-C atom was removed with the decrease of ΔG to 0.36 eV, which led to the formation of the CH_3HC=O@cluster. Then, the H_2O molecule was added producing the $CH_3HC(OH)_2$@cluster, which further lowered ΔG to −0.01 eV. Next, H atom removal from one of the two –OH groups produced the $CH_3HCO(OH)$@cluster. Similar to the aforementioned step, the H of the α-C atom was removed finally leading to the CH_3COOH@cluster with the release of ΔG of 1.06 eV. After the desorption of CH_3-COOH from the $Au_{30}Ag_{12}$ cluster, the CH_3CH_2OH was oxidized to CH_3COOH. Considering the symmetry of the $Au_{47}Ag_{19}$ cluster, 17 possible reactive sites existed. As shown in Fig. S23b,† through calculating the electronic energy change of the removal of the H atom from the O–H group of the adsorptive CH_3CH_2OH, the reactive site with lower energy alternation was applied. Following the identical reaction steps of the $Au_{30}Ag_{12}$ cluster, the whole reaction path leading to CH_3COOH on $Au_{47}Ag_{19}$ can be obtained as depicted *via* the red line of Fig. S24.† The largest ΔG increment of the CH_3CH_2OH oxidation reaction was 0.52 eV, which was lower than that on $Au_{30}Ag_{12}$. This meant that the catalytic performance on $Au_{47}Ag_{19}$ was better, which agreed with the experimental results.

Conclusions

In summary, we report the synthesis mechanism and crystal structures of two intermetallic clusters protected by alkyne ligands: $Au_{30}Ag_{12}(C≡CR)_{24}$ exhibits a fantastic $Au_{18}Ag_8$ kernel that is fused by four interpenetrating $Au_{10}Ag_3$ icosahedra, while

$Au_{47}Ag_{19}(C\equiv CR)_{32}$ exhibits a layered Au_{19} core capped by a $Au_{12}Ag_{19}$ shell. Our investigation demonstrates that one stable icosahedron-based cluster transforming into another hcp-like cluster by simple reduction is feasible, which can enrich the library of metal clusters. We also demonstrate that the atom-packing matching and cooperative effect of intermetallic compounds within the two different clusters play a pivotal role in tailoring the molecular exciton state and catalytic properties. We foresee that this work provides new design rules for atomically precise intermetallic nanomaterials.

Data availability

The data are provided in the ESI.†

Author contributions

Y. Z. conceived the work. S. T. prepared the clusters and solved their single-crystals. E. W. and Y. G. performed the calculations. Y. W. and M. Z. performed the TA measurement. T. S., X. C. and W. D. gave helpful suggestions. All authors interpreted the data and co-wrote the manuscript.

Conflicts of interest

There are no conflicts to declare.

Acknowledgements

References

1 R. Jin, G. Li, S. Sharma, Y. Li and X. Du, Chem. Rev., 2021, 121, 567–648.

2 R. Jin, C. Zeng, M. Zhou and Y. Chen, Chem. Rev., 2016, 116, 10346–10413.

3 Z. Lei, X. Wan, S. Yuan, Z. Guan and Q. Wang, Acc. Chem. Res., 2018, 51, 2465–2474.

4 I. Chakraborty and T. Pradeep, Chem. Rev., 2017, 117, 8208–8271.

5 R. Murray, Chem. Rev., 2008, 108, 2688–2720.

6 T. Laaksonen, V. Ruiz, P. Liljeroth and B. Quinn, Chem. Soc. Rev., 2008, 37, 1836–1846.

7 Y. Li, T. Higaki, X. Du and R. Jin, Adv. Mater., 2020, 32, 1905488.

8 X. Cai, G. Li, W. Hu and Y. Zhu, ACS Catal., 2022, 12, 10638–10653.

9 M. Zhu, C. Aikens, F. Hollander, G. Schatz and R. Jin, J. Am. Chem. Soc., 2008, 130, 5883–5885.

10 M. Heaven, A. Dass, P. White, K. Holt and R. Murray, J. Am. Chem. Soc., 2008, 130, 3754–3755.

11 H. Qian, W. Eckenhoff, Y. Zhu, T. Pintauer and R. Jin, J. Am. Chem. Soc., 2010, 132, 8280–8281.

12 C. Zeng, Y. Chen, K. Kirschbaum, K. Appavoo, M. Sfeir and R. Jin, Sci. Adv., 2015, 1, e1500045.

13 S. Yamazoe, S. Takano, W. Kurashige, T. Yokoyama, K. Nitta, Y. Negishi and T. Tsukuda, Nat. Commun., 2016, 7, 10414.

14 R. Jin, C. Liu, S. Zhao, A. Das, H. Xing, C. Gayathri, Y. Xing, N. Rosi, R. Gil and R. Jin, ACS Nano, 2015, 9, 8530–8536.

15 G. Schmid, R. Pfeil, R. Boese, F. Bandermann, S. Meyer, G. Calis and W. Vandervelden, Chem. Ber., 1981, 114, 3634–3642.

16 Y. Shichibu, Y. Negishi, T. Watanabe, N. Chaki, H. Kawaguchi and T. Tsukuda, J. Phys. Chem. C, 2007, 111, 7845–7847.

17 R. Jin, C. Liu, S. Zhao, A. Das, H. Xing, C. Gayathri, Y. Xing, N. Rosi, R. Gil and R. Jin, ACS Nano, 2015, 9, 8530–8536.

18 Y. Song, F. Fu, J. Zhang, J. Chai, X. Kang, P. Li, S. Li, H. Zhou and M. Zhu, Angew. Chem., Int. Ed., 2015, 54, 8430–8434.

19 Y. Tan, Y. Lv, L. Xu, Q. Li, J. Chai, S. Yang, H. Yu and M. Zhu, J. Am. Chem. Soc., 2023, 145, 4238–4245.

20 M. Zhou, K. Li, P. Wang, H. Zhou, S. Jin, Y. Pei and M. Zhu, Nanoscale, 2023, 15, 2633–2641.

21 J. Hu, M. Zhou, K. Li, A. Yao, Y. Wang, Q. Zhu, Y. Zhou, L. Huang, Y. Pei, Y. Du, S. Jin and M. Zhu, Small, 2023, 19, 2301357.

22 Y. Shichibu and K. Konishi, Small, 2010, 6, 1216–1220.

23 A. Das, C. Liu, H. Y. Byun, K. Nobusada, S. Zhao, N. Rosi and R. Jin, Angew. Chem., Int. Ed., 2015, 54, 3140–3144.

24 T. Higaki, C. Liu, C. Zeng, R. Jin, Y. Chen, N. Rosi and R. Jin, Angew. Chem., Int. Ed., 2016, 55, 6694–6697.

25 Y. Li, Y. Song, X. Zhang, T. Liu, T. Xu, H. Wang, D. Jiang and R. Jin, J. Am. Chem. Soc., 2022, 144, 12381–12389.

26 B. Teo, X. Shi and H. Zhang, J. Am. Chem. Soc., 1992, 114, 2743–2745.

27 P. Pan, C. Zhou, H. Li, C. Zhu, C. Chen, X. Kang and M. Zhu, Nanoscale, 2021, 13, 17162–17167.

28 Z. Guan, F. Hu, J. Li, Z. Wen, Y. Lin and Q. Wang, J. Am. Chem. Soc., 2020, 142, 2995–3001.

29 W. Fan, Y. Yang, Q. You, J. Li, H. Deng, N. Yan and Z. Wu, J. Phys. Chem. C, 2023, 127, 816–823.

30 Q. Li, S. Yang, T. Chen, S. Jin, J. Chai, H. Zhang and M. Zhu, Nanoscale, 2020, 12, 23694–23699.

31 J. Wang, Z. Wang, S. Li, S. Zang and T. Mak, Angew. Chem., Int. Ed., 2021, 60, 5959–5964.

32 S. Chen, L. Xiong, S. Wang, Z. Ma, S. Jin, H. Sheng, Y. Pei and M. Zhu, J. Am. Chem. Soc., 2016, 138, 10754–10757.

33 Q. Li, T. Luo, M. Taylor, S. Wang, X. Zhu, Y. Song, G. Mpourmpakis, N. Rosi and R. Jin, Sci. Adv., 2017, 3, e1603193.

34 S. Zhang, Y. Li, L. Feng, Q. Xue, Z. Gao, C. Tung and D. Sun, Nano Res., 2021, 14, 3343–3351.

35 Q. Yao, X. Yuan, V. Fung, D. Leong, D. Jiang and J. Xie, Nat. Commun., 2017, 8, 927.

36 S. Wang, H. Abroshan, C. Liu, T. Luo, M. Zhu, H. Kim, N. Rosi and R. Jin, Nat. Commun., 2017, 8, 848.

37 G. Guisbiers, R. Mendoza-Cruz, L. Bazán-Díaz, J. Velázquez-Salazar, R. Mendoza-Perez, J. Robledo-Torres, J. Rodriguez-Lopez, J. Montejano-Carrizales, R. Whetten and M. José-Yacamán, *ACS Nano*, 2016, **10**, 188–198.

38 L. Deng, W. Hu, H. Deng, S. Xiao and J. Tang, *J. Phys. Chem. C*, 2011, **115**, 11355–11363.

39 M. Zhou, T. Higaki, G. Hu, M. Sfeir, Y. Chen, D. Jiang and R. Jin, *Science*, 2019, **364**, 279–282.

40 W. Tian, W. Si, S. Havenridge, C. Zhan, Z. Wang, C. Aikens, C. Tung and D. Sun, *Sci. Bull.*, 2024, **69**, 40–48.

41 W. Si, C. Zhang, M. Zhou, W. Tian, Z. Wang, Q. Hu, K. Song, L. Feng, X. Huang, Z. Gao, C. Tung and D. Sun, *Sci. Adv.*, 2023, **9**, 3587.

42 D. Hibbitts and M. Neurock, *J. Catal.*, 2013, **299**, 261–271.

43 E. Monyoncho, S. Steinmann, C. Michel, E. Baranova, T. Woo and P. Sautet, *ACS Catal.*, 2016, **6**, 4894–4906.